Copper(II)-porphyrin functionalized titanium(IV) metal-organic aerogels for the visible-light driven conversion of CO_2 to alcohols

Maite Perfecto-Irigaray [a], Ivan Merino-Garcia [b], Jonathan Albo [b], Garikoitz Beobide [a, c, *], Oscar Castillo [a, c], Antonio Luque [a, c], Sonia Pérez-Yáñez [a, c, **]

[a] Department of Organic and Inorganic Chemistry, University of the Basque Country, UPV/EHU, P.O. 644, Bilbao E-48080, Spain
[b] Departamento de Ingenierías Química y Biomolecular, Universidad de Cantabria, Avda. Los Castros S/n, Santander 39005, Spain
[c] BCMaterials, Basque Center for Materials, Applications and Nanostructures, UPV/EHU Science Park, Leioa 48940, Spain

ABSTRACT

This manuscript covers the synthesis and characterization of a series of titanium based metal-organic aerogels (MOAs) functionalized with copper(II)-metalated porphyrins for their application in visible-light-driven carbon dioxide (CO_2) conversion to alcohols. A thorough characterization is performed using a set of spectroscopic and microstructural analysis techniques to reveal the structural and microstructural features that can aid in establishing structure-activity relationships. The parent MOAs consist of metal-organic nanoparticles (5−10 nm) crosslinked into a highly porous microstructure (surface area: 600−800 $m^2 \cdot g^{-1}$). The post-synthetic reaction with copper(II) enables the metalation of the tetrapyrrole ring of porphyrin, which is confirmed by analyzing the absorption and luminescence spectra. High-angle annular dark-field electron microscopy imaging demonstrates a uniform distribution of the metalation throughout the nanoparticles that compose the material. The CO_2 photoreduction experiments performed in an optofluidic microreactor show that the metalation markedly invigorates the total alcohol (methanol and ethanol) production rates and apparent quantum yields (AQY), from 21 to 367 $\mu mol \cdot g^{-1} \cdot h^{-1}$ (AQY: 0.4−7%) prior to metalation to values of 356−642 $\mu mol \cdot g^{-1} \cdot h^{-1}$ (AQY: 11−20%). Additionally, the metalation inverts the selectivity towards ethanol, increasing from 0−12% in the parent MOA to 67−76% after incorporating Cu(II).

© 2023 The Authors. Published by Elsevier Ltd. This is an open access article under the CC BY-NC-ND license (http://creativecommons.org/licenses/by-nc-nd/4.0/).

1. Introduction

The technologies for carbon dioxide (CO_2) conversion into value-added products, including chemical feedstock and fuels, are experiencing a burgeoning scientific and industrial activity, boosted by environmental concerns about global warming and by the ambitious plans that are emerging worldwide [1,2]. Several methods are applicable in the transformation of CO_2, such as chemical, thermochemical, electrochemical, biochemical, and photochemical methods [3]. Among them, the photocatalytic reduction of CO_2 has the potential of reusing waste without requiring more energy than that offered by the product obtained, which aligns well with the circular chemistry strategies that can enable the circular economy aimed at a sustainable society [4]. In this context, alcohols such as methanol (CH_3OH) and ethanol (C_2H_5OH) are very valuable products that can be produced through the photoreduction of CO_2. However, high-performing and selective production of CH_3OH (6 e^- reduction) and of C_2H_5OH (12 e^- reduction) by photochemical methods is a demanding chemical challenge that still requires further progress in both photocatalyst and reactor design [5]. Most intensely studied heterogeneous photocatalysts consist of UV-active wide-band gap inorganic semiconductors, although materials with band gap energy fitting the visible light range have the potential to maximize photocharge production under sunlight illumination. To overcome the limitations in the potential of complementary reduction/oxidation photoreactions that visible-active narrow band gap materials might present, strategies such as metal/non-metal doping, heterojunction formation, photosensitizer anchoring, or the use of sacrificial reagents have been proposed [5]. In recent years, metal-organic frameworks (MOFs) have emerged as an alternative to inorganic

* Corresponding author.
** Corresponding author.
E-mail addresses: garikoitz.beobide@ehu.eus (G. Beobide), sonia.perez@ehu.eus (S. Pérez-Yáñez).

photocatalysts in light-assisted CO_2 reduction. These MOFs have shown the ability to generate various products, including methanol, ethanol, acetaldehyde, and carbon monoxide, among others [6–11]. It is worth noting that MOFs have a versatile chemical and electronic structure that can be tuned by the assembly of rationally selected building blocks, which allows them to direct their functionalities, such as catalytic behavior or light-absorption properties. Besides, MOFs feature a nanoporous framework with a high surface-area-to-volume ratio, which provides great CO_2 adsorption capacity and reduces the mean path to surface for photogenerated charges. More recently, CO_2 photocatalytic reduction has been assessed using metal-organic aerogels (MOAs), whose performances have far exceeded those of analogous microcrystalline MOFs [12]. These emerging materials [13] exhibit a meso/macroporous microstructure that implies a more fluent diffusion of reagents and products than the one provided by the narrower intrinsic pores of MOFs, and as a result, the reaction kinetics can be improved.

Another remarkable feature of MOAs relies on their synthesis, which is performed by controlling the polymerization of the metal-organic entities in such a way that a rapid nucleation yields an initial colloid that evolves into a metal-organic gel. Such a rapid nucleation provides the opportunity of dispensing with the high selectivity of the building blocks imposed by the growth of a crystalline framework, and thus, it has the potential to spread the variety of the structural entities that comprise the polymeric framework. Exploiting this fact, we have been able to tune the synthesis conditions to yield a novel family of aerogels based on titanium(IV) and 2-aminobenzene-1,4-dicarboxylato linkers, incorporating controlled ratios of a meso-substituted porphyrin. The amino-functionalization of the linker has been chosen based on the proven affinity of this group towards CO_2 adsorption [14], while the tetrapyrrole ring of the porphyrin is a suitable site to carry out metalation reactions. Note that metalloporphyrins are ubiquitous co-factors in enzymes that govern multiple biological catalytic and photocatalytic processes that have also been widely explored in chemical synthesis [15,16]. In the current study, the metalation of the porphyrin involves the post-synthetic reaction with copper(II) which is crucial to the performance and product selectivity of the light-driven CO_2 photoreduction.

2. Materials and methods

2.1. Synthetic procedures

2.1.1. Reagents

All the chemicals were of reagent grade and were commercially obtained. Titanium(IV) n-butoxide (Sigma-Aldrich, 98%, 1.00 g·mL^{-1} at 20 °C), 2-aminobenzene-1,4-dicarboxylic acid (H_2NH_2BDC, Sigma-Aldrich, 99%), meso-tetra(4-carboxyphenyl) porphine (H_4TCPP, Apollo Scientific, 97%), hydrochloric acid (HCl, Labkem, 35–38%), butan-2-ol (Sigma-Aldrich, 99%), N,N-dimethylformamide (DMF, Labkem, 99.9%), ethanol absolute (Scharlab), copper(II) nitrate hemi(pentahydrate) (Sigma-Aldrich, 98%).

2.1.2. Synthesis of the metal-organic aerogels

Synthesis of metal-organic gels (MOGs). Firstly, 1114 μL of titanium(IV) n-butoxide (3.18 mmol) were added to 10 mL of butan-2-ol, and after 5 min of mixing, 118 μL of HCl 0.29 M dissolved in 4 mL of butan-2-ol were added dropwise. The resulting clear solution was stirred for an hour in a sealed vessel. Afterwards, a DMF/butan-2-ol (10 mL/2 mL) solution containing H_2NH_2BDC (0.4355 g, 2.38 mmol) and different amounts of H_4TCPP (Table 1) was added, obtaining stable sols. The total amount of dicarboxylic ligand was

set to achieve a titanium:linker molar ratio of 1:0.75, according to the ideal ratio found in MIL-125-NH_2 MOF [17]. The mixture was introduced into a preheated oven within a closed vessel and maintained at 80 °C for 6 h. As a result, well-formed reddish metallogels were obtained. The gels were robust enough to maintain the shape of the vessel and to be processed as monolithic shapes using cutting tools (Fig. S1). The remaining reagents were removed by exchanging the solvent trapped in the gels with a mixture of butan-2-ol/DMF (2:1), followed by a mixture of butan-2-ol/DMF/absolute ethanol (1:1:1), and finishing with three exchanges of absolute ethanol to obtain the alcogels.

Post-synthetic metalation with copper(II). The three porphyrin-based MOGs were subjected to a copper(II)-doping process. For this purpose, 5 g of the alcogels were placed in a closed vessel within 100 mL of a copper(II) nitrate solution in absolute ethanol. The Cu(II) concentrations varied depending on the measured TCPP content of the gels to provide one copper for each porphyrinic ligand (Table 1). The process was prolonged for 12 h in a closed vessel. Afterwards, the MOGs were recovered and exchanged with absolute ethanol three times.

Preparation of metal-organic aerogels (MOAs). The metal-organic aerogels were prepared by subjecting the gels to a supercritical drying procedure. This procedure was performed using an E3100 critical point dryer from Quorum Technologies, which allowed the replacement of the ethanol with air without destroying the nanostructured pore network. First, the MOGs were immersed in liquid CO_2 at 20 °C and 50 bar for 1 h to exchange the ethanol. Afterwards, the exchanged alcohol was removed through the purge valve, and the process was repeated three times. Then, they were dried under supercritical conditions by increasing the temperature and pressure to 40 °C and 85 bar (above the carbon dioxide critical point: 31 °C and 74 bar) and finally, under constant temperature (40 °C), the chamber was slowly vented up to atmospheric pressure. Metal-organic xerogels (MOXs) were prepared by drying the alcogels in an oven for 2 h at 150 °C. Thereafter, the xerogels were outgassed under vacuum at 150 °C for 4 h to ensure the removal of any remaining solvent molecules, prior to the chemical characterization of the material. MOAs maintain almost the same shape with a slight contraction (≤25%) that takes place in the supercritical drying procedure, whereas MOXs greatly reduce their size and present several cracks due to the collapse of the porous microstructure during the conventional oven drying procedure.

2.2. Characterization

2.2.1. Chemical characterization

Powder X-ray diffraction (PXRD) measurements were performed at 20 °C on a Phillips X'PERT diffractometer (Cu-K$_\alpha$ radiation, $\lambda = 1.5418$ Å) over the 5–70° 2θ range with a step size of 0.02°, a variable automatic divergence slit, and an acquisition time of 2.5 s per step. Attenuated total reflectance Fourier-transform infrared (ATR-FTIR) spectra of the solid samples were recorded at a resolution of 4 cm^{-1} in the 4000–600 cm^{-1} region using a FTIR 8400S Shimadzu spectrometer equipped with an ATR accessory. Thermogravimetric analyses (TGA) were performed on a METTLER TOLEDO TGA/SDTA851 thermal analyzer in synthetic air (80% N_2, 20% O_2) with a flux of 50 cm^3·min^{-1}, from room temperature to 800 °C with a heating rate of 5 °C·min^{-1} and a sample size of about 15 mg per run. Proton nuclear magnetic resonance (^{1}H-NMR) spectra were acquired in a Bruker AVANCE 5OO (one-bay; 500 MHz) at 20 °C. Prior to the measurement, samples were digested in 2 mL of a 1 M NaOH (Sigma-Aldrich, 98%) solution in deuterated water (D_2O, Sigma Aldrich, 99%). The digestion was prolonged for 1 h, after which fumaric acid (Sigma-Aldrich, +99%) was added as internal patron, the solid residue was filtered off, and

Table 1
Sample coding and amounts of H_4TCPP ligand and copper(II) employed during the synthesis and metalation of $Ti/NH_2BDC/TCPP$ gels.[a]

Sample code	MOGs synthesis			Cu-doping process	Post-doping code
	H_4TCPP amount		Ti:TCPP ratio	$Cu(NO_3)_2$ solution (mM)	
	g	mmol			
TCPP_0.01	0.0032	0.0040	8:0.01	0.008	Cu@TCPP_0.01
TCPP_0.1	0.0324	0.0397	8:0.1	0.119	Cu@TCPP_0.1
TCPP_1	0.3235	0.3969	8:1	0.768	Cu@TCPP_1

[a] The number provided in the sample codes indicates the synthesis ratio of TCPP per Ti_8O_8 core.

the NMR spectrum was taken on the liquid fraction. UV−Vis absorption spectra of the filtrate of the overnight (12 h) digested samples in 1 M NaOH solution were collected using quartz cuvettes in a Jenway 6705 UV/Vis spectrophotometer within the spectral range of 300−800 nm. X-ray fluorescence (XRF) analysis of doped samples was made in a PANalytical sequential wavelength dispersive X-ray fluorescence spectrometer (WDXRF, AXIOS model) equipped with a Rh tube and three detectors (gas flow scintillation and Xe sealing). X-ray photoelectron spectroscopy (XPS) measurements were performed on a Phoibos 150 1D-DLD (SPECS) energy analyzer equipped with a Focus 500 monochromatic radiation source, an Al/Ag dual anode, and a SED-200 secondary electron detection system.

2.2.2. Electrospray ionization mass spectrometry

Electrospray ionization mass spectrometry (ESI-MS) measurements were performed in a high-resolution mass spectrometer (Synapt G2 from Waters Cromatografia S.A., time of flight (TOF) analyzer) equipped with an electrospray ionization source in positive and negative modes. The high-resolution spectra were recorded in scan mode, with a mass range of 30−1200 Da in resolution mode (FWHM ≈ 20 000) and a scan time of 0.1 s. The source and desolvation temperatures were 120 and 350 °C, respectively. The capillary voltage was set to 2.5 kV (negative), while the cone voltage was maintained at 15 V. N_2 was used as desolvation and cone gas, with flow rates of 600 and 10 $L \cdot h^{-1}$. Prior to analysis, the mass spectrometer was calibrated using a sodium formate solution and a leucine-enkephalin solution for the lock mass correction, monitoring the ions at a mass-to-charge ratio (m/z) of 556.2771. All of the acquired spectra were automatically corrected during acquisition based on the lock mass.

2.2.3. Electron microscopy

Scanning electron microscopy (SEM) images were obtained in the FEG-SEM JEOL 7000F system, in secondary electron (SE) and backscattered electron (BSE) modes, at magnifications between ×200 and ×200 k, using an accelerating voltage of 10 kV, a current intensity of 0.1 nA, and an approximate working distance of 10 mm. The samples for SEM were adhered to the sample holder using double-sided adhesive carbon tape and coated with a Cr layer (20 nm) by sputtering using the Q150T sample preparation kit (Quorum Technologies Ltd.). Transmission electron microscopy (TEM) studies were done in a TECNAI G2 20 TWIN system, operated at 200 kV and equipped with a LaB_6 filament, a brightfield/darkfield detector, and an X-ray microanalysis unit (EDX). The samples for room temperature TEM were prepared by a dry dispersion of the aerogels onto a TEM copper grid (300 mesh) covered by a holey carbon film.

2.2.4. Dinitrogen and carbon dioxide adsorption measurements

N_2 (77 K) and CO_2 (273 and 298 K) physisorption data were recorded with a Quantachrome Autosorb-iQ MP analyzer. Prior to measurements, all samples were outgassed under vacuum at 140 °C

for 6 h. The surface area values were obtained by fitting the N_2 adsorption data to the Brunauer-Emmett-Teller (BET) equation [18]. In order to choose the appropriate pressure range and to avoid ambiguity when reporting the BET surface area, we used the three consistency criteria proposed by Rouquerol et al.: (1) the pressure range selected should have values of V (1-p/p°) increasing with p/p°, (2) the points used to calculate the BET surface area must be linear with an upward slope in such a way that the linear regression must yield a positive y-intercept (i.e. a positive C value), and (3) the p/p° value corresponding to V_m should be within the BET fitting range [19]. To estimate CO_2 adsorption enthalpies (Q_{st}), the isotherms were fitted to the modified Clausius−Clapeyron equation [20,21]. The micropore volume of the samples was estimated according to the t-plot method [22,23].

2.2.5. Optical characterization

Fluorescence spectroscopy measurements were performed on a Varian Cary Eclipse (Agilent Technologies) optical spectrometer, equipped with a 450 W Xenon flash lamp, a monochromator, and a 90°−located photomultiplier (PMT). The measurements performed in emission scan mode were recorded in the 600−900 nm range using an excitation wavelength of 420 nm, an 800 V PMT, and a 600 $nm \cdot min^{-1}$ scan rate. Diffuse reflectance UV−Vis spectroscopy (DRS-UV-Vis) analysis was carried out in a Cary 7000 (Agilent Technologies), equipped with tungsten halogen (visible) and deuterium arc (UV) light sources. The spectra were recorded in reflectance mode in the 300−800 nm range and with a 600 $nm \cdot min^{-1}$ scan rate. The UV−visible diffuse reflectance spectra of the samples were transformed to the corresponding absorption spectra by applying the Kubelka−Munk function: $F(R) = (1−R_\infty)^2/(2 R_\infty)$ ($R_\infty = R_{sample}/R_{standard}$, is the reflectance) [24,25].

2.2.6. Photoreduction of CO_2 in a planar optofluidic microreactor

The photoreactor consists of a home-made planar optofluidic microreactor (APRIA Systems S.L.) equipped with a reaction microchamber of 1 cm^2 and 75 μL that provides a high surface-area-to-volume ratio, uniform light distribution, and enhanced mass transfer for the continuous light-driven transformation of CO_2 [26]. A porous carbon paper (Toray TGP-H-60) containing the MOA is sandwiched with polytetrafluoroethylene (PTFE) gaskets between two highly transparent (light transmission of 90% at λ > 365 nm) polymethylmethacrylate(PMMA) (Altuglas-Arkema) plates, and a stainless-steel plate on top (Fig. S12). The preparation of the light-responsive surfaces has been carried out following a previously reported procedure [27]. Accordingly, the light-responsive supports were prepared by airbrushing a catalytic ink onto a teflonated porous carbon paper (Toray TGP-H-60). This ink was comprised by the corresponding MOA, a 5 wt% Nafion dispersion as a binder, and isopropanol as a vehicle, with a catalyst/Nafion mass ratio of 70/30 and a 3% solids (catalyst + Nafion) percentage. Prior to airbrushing, the ink was sonicated for 30 min to obtain a homogeneous slurry. The airbrushing process was carried out at 100 °C to ensure the complete evaporation of the solvent

during the accumulation of photocatalytic layers. The total MOA mass loading per photoelectrode was set to 2 mg·cm^{-2}, which is experimentally determined by continuous weighing. The opto-fluidic microreactor is placed in a ventilated dark box, and the temperature is controlled with an infrared thermometer (*ca.* 20 °C). During the light-driven process, the microchamber is irradiated with LED lights (peak at 450 nm; Fig. S13) with a light intensity of E = 5 mW·cm^{-2} measured by a radiometer (Photoradiometer Delta OHM) and controlled by adjusting the visible LED intensity and the distance between the microreactor and the LED. A CO_2 saturated 0.5 M $KHCO_3$ aqueous solution (pH = 7.38 ± 0.03) prepared with ultra-pure water (18.2 MΩ·cm at 273 K, MilliQ Millipore system) was supplied to the microchamber with a peristaltic pump (Mini-puls 3 Gilson) at a flow rate of Q_L = 100 μL·min^{-1}. The photo-chemical CO_2 reduction tests for each photoactively prepared material were carried out in duplicate in continuous mode for 180 min, when a pseudo-stable performance was reached. Blank tests using a 0.5 M $KHCO_3$ aqueous solution without bubbling CO_2 (pH = 8.29 ± 0.04) and/or using dark reaction conditions were also performed. The concentration of alcohols in each sample was analyzed in duplicate in a headspace gas chromatograph (GCMS-QP2010 Ultra Shimadzu) equipped with a flame ionization detector (FID). An average concentration was obtained for each point. The apparent quantum yield (AQY) values have been calculated using equation (1):

$$AQY = \frac{n_e}{n_p} \bullet 100 \qquad\qquad 1$$

where n_e represents the rate of electrons required for CH_3OH and C_2H_5OH formation, defined as the number of evolved molecules (mol) multiplied by the number of reacted electrons (6 and 12 e$^-$ for CH_3OH and C_2H_5OH, respectively) and the Avogadro number (mol^{-1}). The denominator, n_p, implies the rate of incident photons on the surface and is calculated using equation (2):

$$n_p = \frac{E \cdot A \cdot t \cdot \lambda}{h \cdot c} \qquad\qquad 2$$

where E stands for the light intensity (W·m^{-2}), A is the irradiation area (m^2), t is the reaction time (s), λ is the wavelength peak (m), h is the Planck' constant (6.626·10^{-34} J·s) and c corresponds to the speed of light (2.998·10^8 m·s^{-1}).

3. Results and discussion

3.1. Chemical and spectroscopic characterization

To analyze the nuclearity of the titanium oxo-clusters present in the metal-organic network, electrospray ionization mass spectrometry (ESI-MS) was performed in the stable solutions obtained prior to and after the addition of carboxylic ligands. The peaks found in the spectra have allowed us to identify the formula of the species formed using the ChemCalc platform [28], while MassLynx software [29] was employed to simulate the spectra of each identified species. The collation of the measured and simulated spectra is shown in Fig. 1 and Fig. S2, while the corresponding *m/z* values and other agreement figures for each complex are gathered in Table S1. Note that the intensity of the computed peaks is equal and normalized to the maximum intensity as the simulation cannot deal with the concentration of the species. Both ESI(+)-MS measurements evidence the presence of a series of Ti_8O_8 clusters with differences in the amount of water and solvent molecules that directly affect the position of the peak of each species. The addition of the carboxylic ligands to the reaction media affects the relative

intensity of the peaks in the spectrum (Fig. S2), which is related to the concentration change of the complexes in the solution. This change seems to be related to the water added along with the DMF solution of ligands, as those peaks that disappear or reduce their intensity are related to species with lower relative water content. The herein observed type of octanuclear Ti_8O_8 clusters are also commonly found in Ti/carboxylate-based discrete complexes and MOFs [30,31], as is the case of the well-known MIL-125 and MIL-125-NH$_2$, both featured by the chemical formula $[Ti_8O_8(OH)_4L_6]_n$ (L: benzene-1,4-dicarboxylate or 2-aminobenzene-1,4-dicarboxylate, respectively).

The addition of the polycarboxylic ligands (NH_2BDC and TCPP) to the reaction mixture prompted the growth of the metal-organic framework into nanoscopic particles that crosslink to yield reddish translucent gels, which are comprised of 96% solvent. The super-critical drying of the MOGs led to a slight contraction, but the resulting MOAs (Fig. 2) featured a markedly low density (0.1 g·cm^{-3}) and high porosity (see below). Chemical analysis combining ^{1}H-NMR and UV−Vis characterization of digested samples with TGA analysis helped us get a bigger insight into the chemical composition of the metal-organic framework (see details of the analyses in the supplementary data). Taking into account the outcomes of the ESI-MS analyses, the chemical formulas were normalized to Ti_8O_8 units (Table 2), considering two possible ways to compensate the linker vacancies: OH$^-$/H_2O pairs and formate (HCOO$^-$ generated from the DMF decomposition during the synthesis).

As it can be observed, each MOA is comprised by 2−3 NH_2BDC linkers per Ti_8O_8 cluster, and the content of TCPP is close to the targeted one. Formate and OH$^-$/H_2O pairs would complete the coordination sphere of the octanuclear clusters to compensate the linker vacancies, as commented before and as usually occurs in defective MOFs of group IV metals [32]. Furthermore, the PXRD patterns (Fig. 3) reveal a broad peak at 2θ = 6−7° which is fairly close to the maximum intensity peak present in the MIL-125-NH$_2$ pattern (2θ = 6.8°). This reflection is related to the interplanar distance set by the NH_2BDC linker between titanium cluster arrays from the combined contributions of (101) and (110) reflections (d_{101} = 12.0 Å; d_{110} = 13.2 Å) [33]. Interestingly, when the TCPP content increases, a second broad maximum emerges at 2θ = 3−4° as observed in the TCPP_1 sample. This maximum corresponds to a spacing of 22.1−29.4 Å which is close to the range of distances set by TCPP ligand among titanium oxo-clusters (centroid···centroid distances: 23.27−27.57 Å) [34−36] in metal-organic structures.

Once the Cu(II)-doping process was performed, copper content was determined by X-ray fluorescence measurements (XRF). The results of Ti and Cu wt% together with the TCPP:Cu ratio are summarized in Table 3. Considering these data, all the tetrapyrrole rings may have been occupied by copper ions in samples Cu@TCPP_0.01 and Cu@TCPP_0.1, whereas in Cu@TCPP_1, 50% of the available positions might be occupied. The copper excess in Cu@TCPP_0.01 and Cu@TCPP_0.1 samples can be explained by the metalation of defective sites of the structure, as commonly occurs in metal-organic frameworks [37]. Contrarily, the decreased efficiency of metalation observed in Cu@TCPP_1 can be attributed to the acidi-fication of the media resulting from the release of protons during complex (Cu^{2+} + TCPP(H_2) ↔ TCPP(Cu) + 2 H$^+$), which would hinder the yield of the metalation at higher reagent concentrations. To corroborate that copper ions were effectively inserted in TCPP ligands, fluorescence spectroscopy measurements were performed (Fig. 4). Prior to metalation, the fluorescence spectra of the parent MOAs show the two fluorescence bands at 650 and 718 nm ascribable to $S_1 \rightarrow S_0$ transitions (excitation wavelength: 420 nm) [38]. In this analysis, it can be observed that the increase in TCPP content produces a self-quenching in the fluorescence emission of
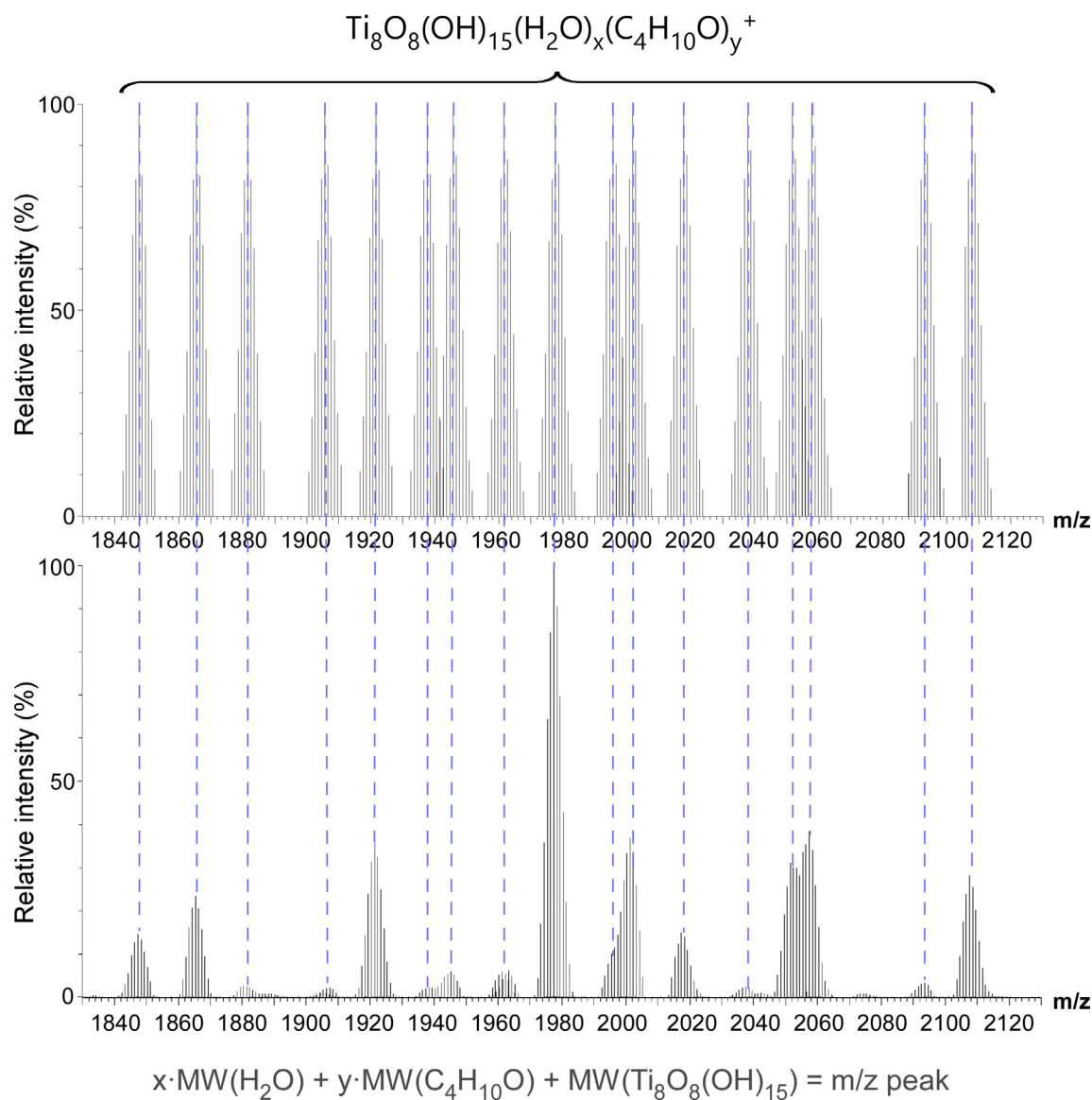
Fig. 1. Comparison between the simulated ESI-MS spectrum (up) and the experimental one (down) for the reaction solution prior to the addition of HCl and bridging ligands.
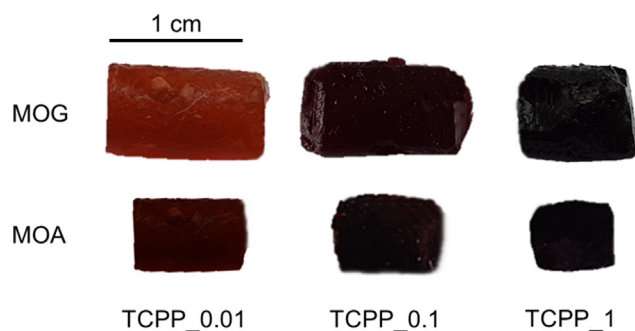
Fig. 2. MOGs and supercritically dried MOAs monoliths.

Table 2
Chemical formula estimated for the synthesized porphyrin-based MOGs.

Sample[a]	Formula
TCPP_0.01	$Ti_8O_8(OH)_4(NH_2BDC)_{2.71}(HCOO)_{0.68}(TCPP)_{0.01}(H_2O)_{5.86}(OH)_{5.86}$
TCPP_0.1	$Ti_8O_8(OH)_4(NH_2BDC)_{2.90}(HCOO)_{0.53}(TCPP)_{0.09}(H_2O)_{5.31}(OH)_{5.31}$
TCPP_1	$Ti_8O_8(OH)_4(NH_2BDC)_{2.13}(HCOO)_{0.71}(TCPP)_{0.70}(H_2O)_{4.23}(OH)_{4.23}$

[a] The number provided in the sample codes indicates the targeted ratio of TCPP per Ti_8O_8 core.

the samples (prior to copper insertion), as can be inferred from the progressive reduction in the maxima relative intensity of fluorescence emission as the TCPP ratio of the pristine materials increases. After the doping process, the two fluorescence bands fall to almost zero in Cu@TCPP_0.01 and disappear in the other two samples. This means that, effectively, copper ions were coordinated to the TCPP macrocycle during the metalation process since Cu(II)-porphyrin complexes are featured by a quenching of the fluorescence due to the unpaired electron present in the $3d_{x^2-y^2}$ orbital of copper [39]. According to density functional calculations performed on metal/meso-tetraphenylporphin complexes [38], the half-filled *d* orbital of Cu(II) lies between the frontier orbitals of the porphyrin, which enables an intramolecular charge transfer that inhibits the radiative relaxation by fluorescence. Fig. 5a depicts the frontier orbitals, which will be further analyzed below in the discussion of absorption properties.
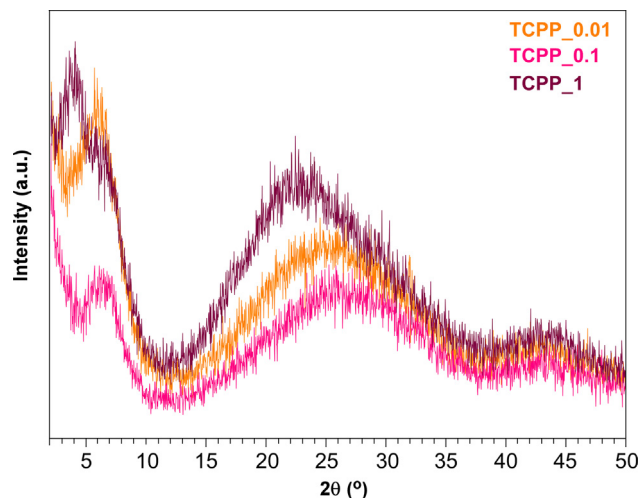
Fig. 3. PXRD patterns of TCPP_0.01, TCPP_0.1 and TCPP_1.

Further evidence of the copper(II)-porphyrin complex was provided by the absorption spectra obtained from DRS-UV-Vis measurements (Fig. 5b). As porphyrins are extended aromatic systems, their absorption bands involve $\pi \rightarrow \pi*$ electronic transitions, and in their UV−Vis absorption spectra, two main regions are distinguished: the area of the so-called Soret or B band (380−500 nm) and the Q band region (500−700 nm). In free-base neutral porphyrins (TCPP(H₂)), i.e. nothing coordinated to the tetrapyrrole macrocycle) with a D_{2h} point group, the Q bands arise from two possible electronic transitions (HOMO → LUMO and HOMO−1 → LUMO, Fig. 5a), in which two different vibrational modes are involved and appear separately in the spectrum, giving as a result four characteristic Q bands. The Soret band, instead, corresponds to electronic transitions to a higher energy unoccupied orbital (LUMO+1) and is usually more intense. The position of these bands shifts depending on the substituents of the porphyrinic ring [40−42].

Accordingly, the absorption spectra of the samples prior to the metalation with copper show the four characteristic Q-bands (651,

Table 3
Titanium and copper content (wt$_M$% of total metal) of doped MOGs and relative TCPP:Cu content.

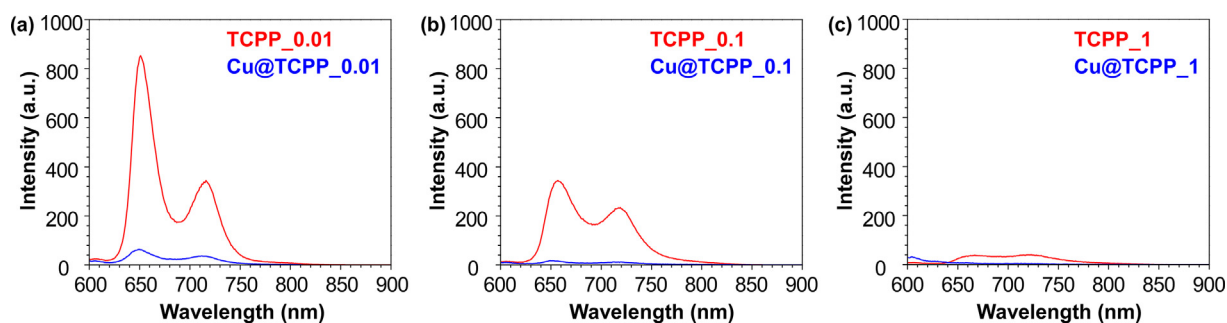| Sample	Relative Ti content (wt$_M$%)	Relative Cu content (wt$_M$%)	TCPP:Cu ratio
Cu@TCPP_0.01	99.85	0.15	1:1.51
Cu@TCPP_0.1	98.15	1.85	1:1.26
Cu@TCPP_1	94.82	5.18	1:0.47

Fig. 4. Comparison of the fluorescence spectra of prepared materials prior to and after the doping process (excitation wavelength 420 nm).
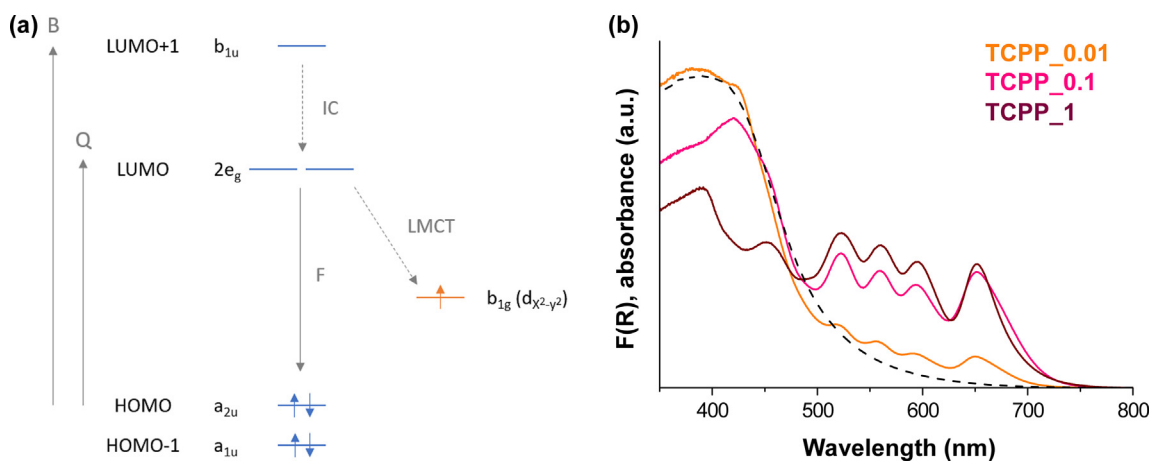

Fig. 5. (a) Simplified molecular orbital diagram for TCPP(Cu) depicting decay pathways: internal conversion (IC), fluorescence (F), and ligand-to-metal charge transfer (LMCT). (b) UV−Vis absorption spectra derived from Kubelka-Munk function for TCPP-based samples compared to those of parent porphyrin-free Ti(IV)/NH₂-BDC samples (dashed line).

594, 559, and 520 nm) whose relative intensity increases with the TCPP(H$_2$) content in the sample. At lower wavelength values, in the 450−500 nm range, the spectra show a steep rise of the absorption, which is ascribed to the $\pi \to \pi*$ transitions of the amino-functionalized BDC linker (see the referential spectrum in Fig. 5b for the metal-organic material lacking TCPP ligand, dashed line). Consequently, the Soret band is not well-defined, but its maximum can be observed in the lower edge of the visible region (420 nm for TCPP_0.01 and TCPP_0.1; 390 and 450 nm for TCPP_1).

A comparison of the UV−Vis spectra of Cu-doped and neat samples is depicted in Fig. 6. As previously reported, the coordination of a metal to the tetrapyrrolic ring leads to a change in molecular symmetry from D$_{2h}$ to D$_{4h}$ and, therefore, the allowed electronic transitions in the Q band region change from two to one, which, in turn, gives rise to two bands instead of four, according to the contribution of two vibrational energy levels [40].
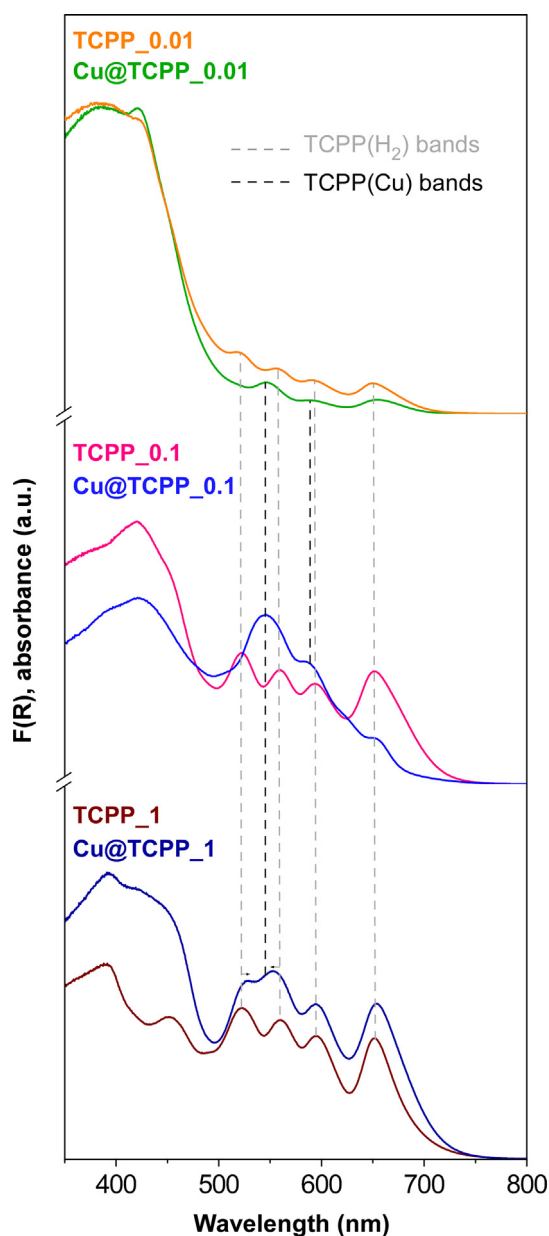

Fig. 6. Absorbance (F(R)) comparison of neat and Cu-doped samples. Q-band maxima of free-base porphyrin bands and Cu(II)-coordinated porphyrin are depicted by grey and black dashed lines, respectively.

For Cu@TCPP_0.01 and Cu@TCPP_0.1 samples, three Q bands are observed: two new signals at 545 and 590 nm that can be related to the copper porphyrin complex, and a third band at 650 nm that matches the band that appears in the free-base spectrum. This band may arise from the fact that a minor percentage of porphyrins are not coordinated to copper, and thus the transition remains visible as the metalloporphyrin bands do not mask it. This conclusion agrees with the aforementioned partial quenching in the fluorescence spectra. In the case of Cu@TCPP_1, the shape, number, and position of the Q bands depict an intermediate situation in which a meaningful amount of both free porphyrin and Cu-porphyrin is present in the sample. Note that since the most intense Q band of TCPP(Cu) lies between the higher in-energy two Q bands of TCPP(H$_2$), their merging in the spectra of the Cu@TCPP_1 sample leads to two maxima slightly shifted to higher and lower energies (552 and 526 nm). The other two maxima maintain their positions (651 and 594 nm) with respect to the free-porphyrin-containing sample. These results agree with the chemical analysis of Cu@TCPP_1, in which the Cu:TCPP ratio is *ca.* 0.5, which indicates roughly half of the porphyrinic ligands remain unmetalated.

To end up with the chemical characterization, X-ray photoelectron spectroscopy (XPS) measurements were performed. The full spectrum for Cu@TCPP_1 is shown in Fig. 7a, whereas the b to f figures present the high-resolution spectra of each of the elements observed with their characteristic components. This analysis allowed us to identify the distinctive 2p peaks of titanium(IV) (2p$_{3/2}$ and 2p$_{1/2}$ at 458.9 and 464.6 eV, respectively) and their three satellite peaks, which fit well with the data available in the literature for MOFs with Ti$_8$O$_8$-type clusters in a hexacoordinated TiO$_6$ environment [43]. Furthermore, the peak observed at 935.2 eV is attributable to the Cu 2p$_{3/2}$ level, and it lies within the common range for Cu(II) compounds [44]. In fact, the binding energy of this signal matches well with that found for Cu(II)-metalloporphyrin-based materials [45]. The intensity of this band is small due to the amount of copper present in the sample in terms of atomic percentage, and for that reason, the other characteristic band of Cu^{2+}, Cu 2p$_{1/2}$, of less intensity, is barely observed (embedded within the noise), and therefore, it is not presented. Finally, the expected C 1s, O 1s, and N 1s bands coming from the organic linkers are observed. In the case of carbon, two C 1s bands at 288.4 eV and 284.6 eV are ascribed to O−C=O and C−C/C−H carbon-types, respectively. Two different environments are also observed for nitrogen, with bands at 398.7 and 401.4 eV that can be attributed to the −NH$_2$ group of the NH$_2$BDC linker and to the nitrogen of the porphyrinic ligand, respectively. The band at 531.1 eV for O 1s comes from the contribution of carboxylic, oxide, and hydroxide ligands [46,47].

3.2. Microstructural characterization

The microstructure of the obtained materials was first studied by transmission electron microscopy (TEM) carried out on MOA samples. The TEM images show that all systems were comprised of partially sintered nanoparticles of *ca.* 5−10 nm (Fig. 8a−c). The random sinterization between them leaves a microstructure featuring mesopores and macropores with a polydisperse size distribution. The microstructure of the MOAs is retained after copper metalation, as shown by the high-angle annular dark-field imaging (HAADF-TEM) of Cu@TCPP_0.1 (Fig. 8d), whereas elemental mapping analysis (Fig. 8e and f) shows a fine and homogeneous distribution of copper, which is consistent with a situation in which copper is coordinated to the metal-organic network instead of clustered within the aerogel microstructure. The mapping of the remaining elements comprising the coordination frameworks (C, N, and O) is gathered in Fig. S10.
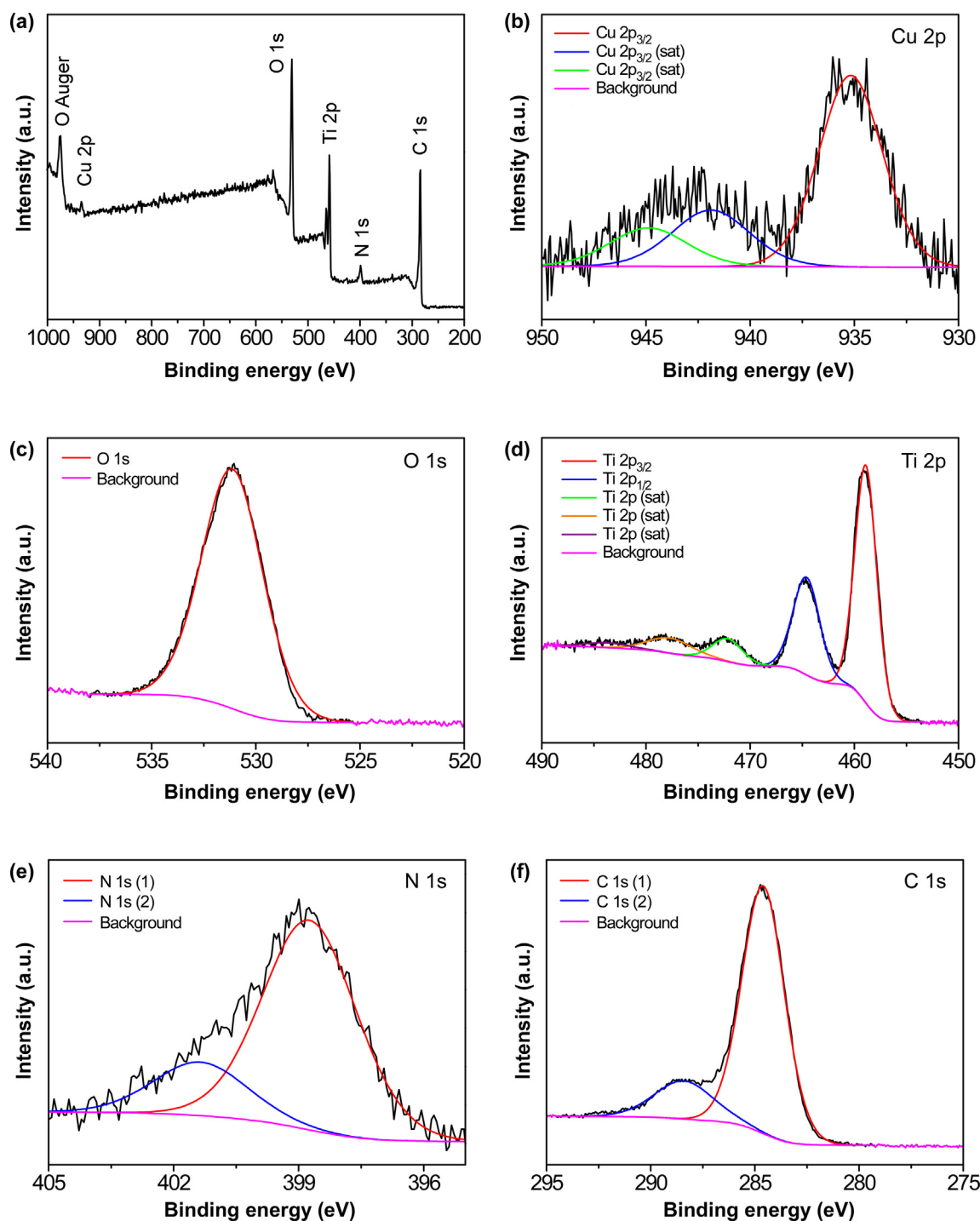
Fig. 7. (a) XPS full spectrum and high resolution spectra for (b) Cu 2p, (c) O 1s, (d) Ti 2p, (e) N 1s, and (f) C 1s peaks of the Cu@TCPP_1 sample. 'Sat' refers to characteristic satellite peaks.

Furthermore, SEM images were also taken on aerogels prior to and after the doping process (Fig. S11). In all cases, we observed a granular, uniform surface with aggregations of nanoparticles of around 50–80 nm.

3.3. Gas physisorption measurements

To get further details of the porosity of the prepared MOAs, N_2 adsorption isotherms at 77 K were measured (Fig. 9). All samples exhibit type II/IV adsorption isotherms following the International

Union of Pure and Applied Chemistry (IUPAC) criteria [48] with a narrow hysteresis loop at relatively high pressures (p/p° > 0.85) as a result of the combination of macropores and mesopores. The data subtracted from the numerical analysis of the curves is gathered in Table 4. The BET surface area of the pristine aerogels ranges from 613 to 822 $m^2 \cdot g g^1$. Despite the fact that these values are lower than those found for the crystalline Ti(IV)-based MOFs of similar linkers (1300–3800 $m^2 \cdot g^{-} g^1$) [49], they can be considered relatively high due to the small particle size and lightness of titanium. In fact, these values overpass those found for analogous
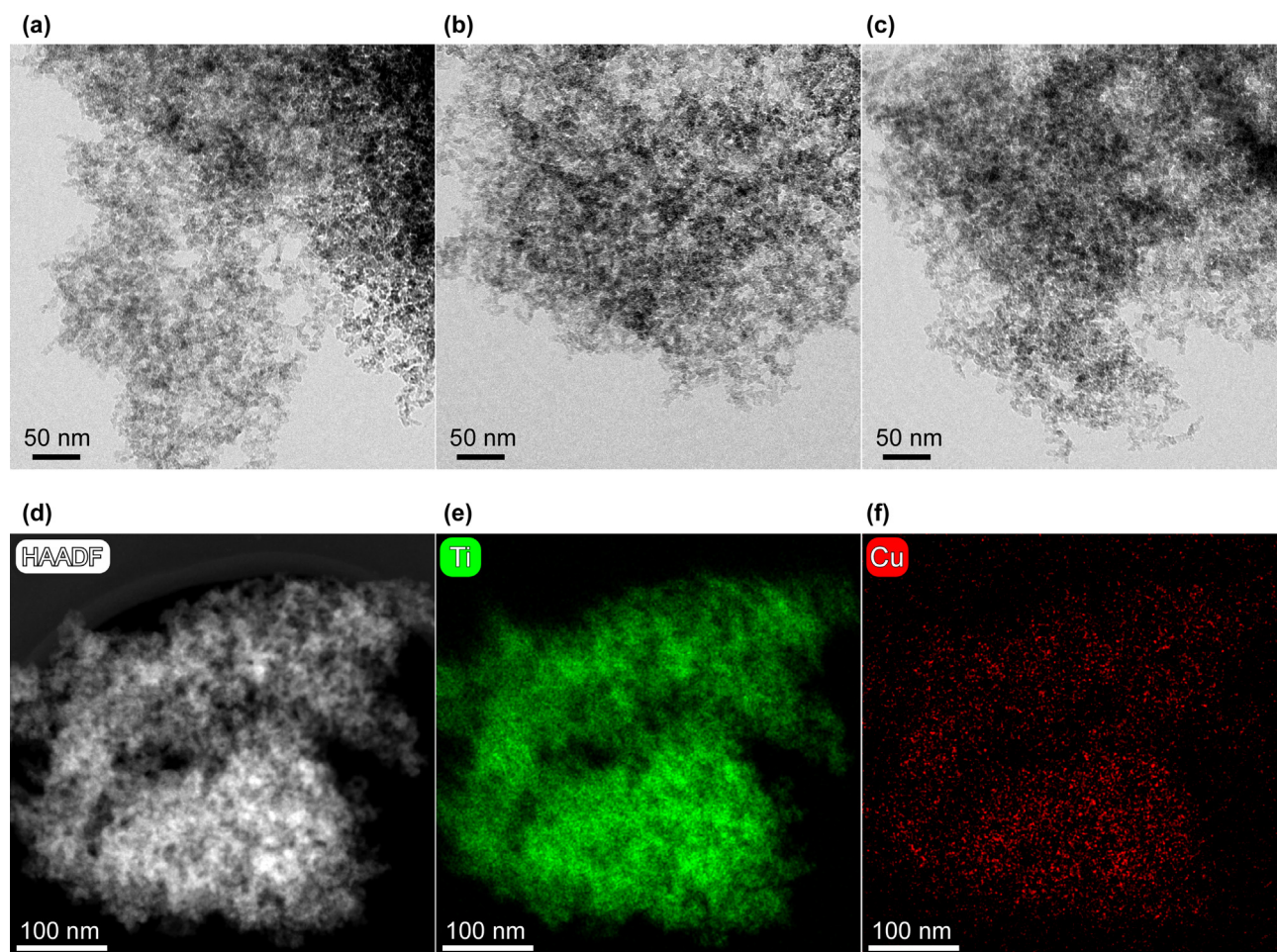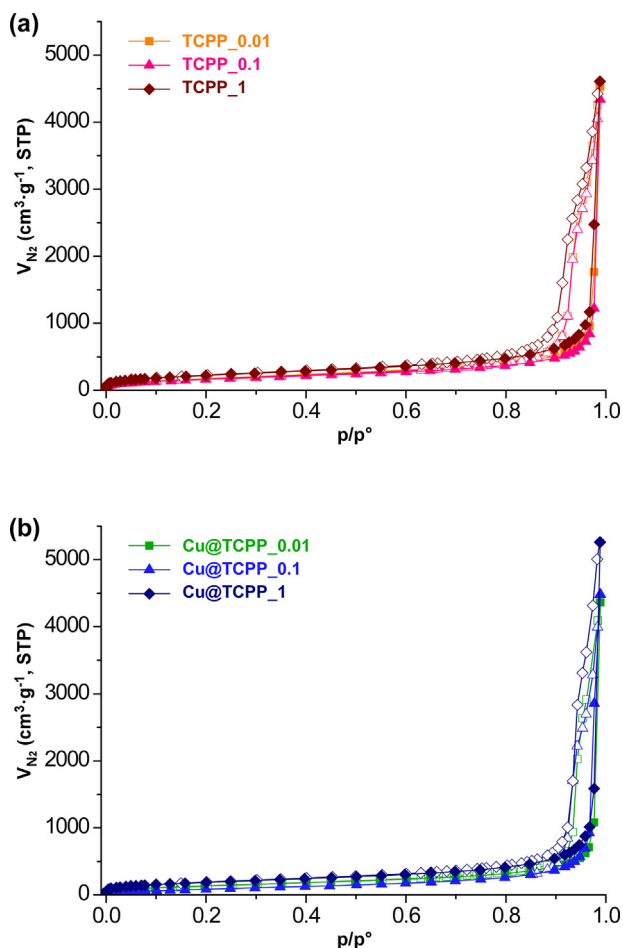
Fig. 8. TEM micrographs of (a) TCPP_0.01, (b) TCPP_0.1, and (c) TCPP_1 aerogels taken at 100 k magnifications. (d) HAADF-TEM micrograph and elemental mapping for (e) Ti and (f) Cu taken on Cu@TCPP_0.1 sample.

zirconium(IV) MOAs (52–377 $m^2 \cdot g^{-1}$) [50]. The pore volume analysis of the samples demonstrates a major contribution of macropores (79–86% of the total porosity), accompanied by a meaningful presence of mesopores (14–21%) and a minor contribution of micropores (<1%). Interestingly, t-plot method analysis of the data reveals that the sample with the greatest porphyrin content (TCPP_1) has a significantly greater contribution of micropores (see S_{micro} and V_{micro} values in Table 4), which explains its notably greater surface area with respect to the aerogels with less TCPP content (TCPP_0.01 and TCPP_0.1). Since non-meaningful microstructural changes were observed in TEM analysis, the increased microporosity can be related to the intrinsic porosity of the particles provided by the large porphyrinic spacer, which, despite the lack of crystallinity, allows to retain certain interconnections between the cavities embedded within the polymeric coordination framework. The metalation with copper(II) produces a slight lowering of the specific surface area and pore volume values, which can be attributed to the increase in density of the MOA. The exception to this statement is the macropore volume, whose value is largely influenced by the p/p° value resulting from the equilibration of the last point of the isotherm. In this sense, small changes in p/p° can probe notably greater or smaller pore ranges, as can be inferred from Table 4 data.

3.4. CO_2 photoreduction experiments under visible light

The alcohol production rates (r_{CH3OH} and r_{C2H5OH}) and apparent quantum yields (AQY) provided by MOAs in the continuous CO_2 photoreduction reaction under visible light are gathered in Fig. 10a and Table S3. Note that the absorption edge related to $\pi \rightarrow \pi^*$ transitions (450–500 nm) of the NH_2BDC linker and Soret (400–500 nm) and Q bands (545–590 nm) of TCPP (Fig. 5) fits well into the visible emission spectra provided by the LED array selected for the photocatalytic experiments (Fig. S13), which could favor a more efficient utilization of the light. A blank test performed in the absence of CO_2 and/or light did not produce any measurable product. The analysis of the liquid fraction showed, in all cases, the formation of both methanol and ethanol, but trace amounts of formic acid were also detected. Formic acid is a plausible intermediate species in CO_2-to-methanol conversion [51]. Although gas-phase products were not herein analyzed, previous studies demonstrated that TiO_2-based catalysts using the same optofluidic microreactor, operating conditions, and visible light irradiation [27,52], led to very low quantities of CO and CH_4 (AQY <0.05%).

The sample TCPP_0.01 produces relatively low amounts of methanol (r_{CH3OH} = 21 μmol$\cdot g^{-1} \cdot h^{-1}$, AQY_{CH3OH} = 0.4%). The previously reported aerogel composed of Ti(IV)−NH_2BDC exhibited

Fig. 9. Nitrogen adsorption isotherms (77 K) for (a) neat and (b) Cu(II)-metalated MOAs. Closed symbols for adsorption curves and open symbols for desorption.

excitonic transfer through the coordination network and prolongs its lifetime [54], which improves the charge transport properties and redox-active of the catalyst [55].
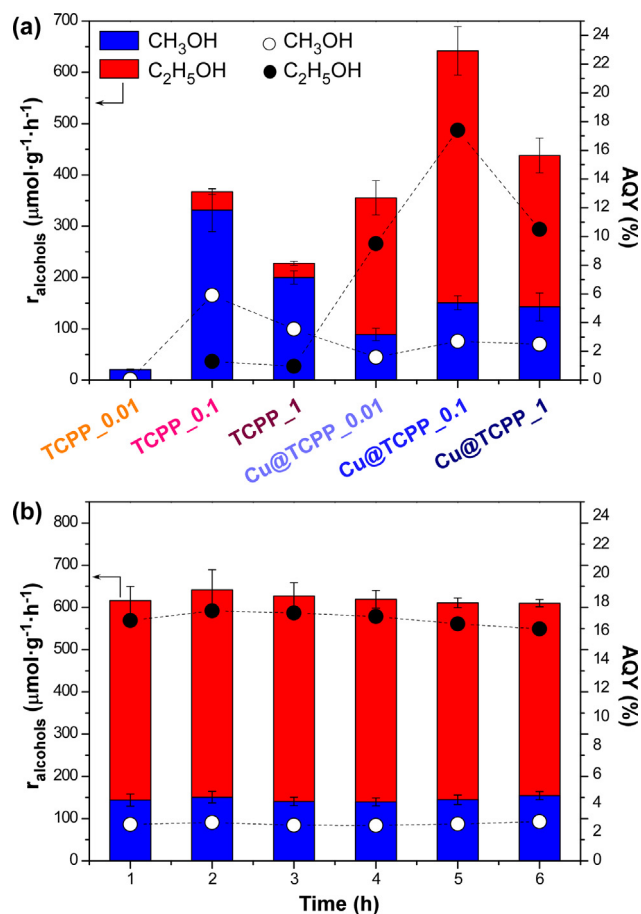
On the other hand, in all cases, the metalation with copper(II) leads to a marked increase in the overall alcohol production, reaching the best performance with Cu@TCPP_0.1 ($r_{alcohols}$: 642 μmol·g^{-1}·h^{-1} and AQY$_{alcohols}$: 20%). As aforementioned, the metalation with copper inhibits the radiative decay and leaves the photoelectron on the metal atom by means of the ligand-to-metal charge transfer mechanism (Fig. 5a). Both factors can be responsible for the performance improvement. Besides, the presence of copper produces a change in product selectivity favoring the formation of ethanol. The maximum rate of ethanol production is attained with Cu@TCPP_0.1, reaching 491 μmol·g^{-1}·h^{-1}. This production rate notably surpasses that of methanol, which stands at 151 μmol·g^{-1}·h^{-1}. Such an inversion of the selectivity can be ascribed to the coordinatively unsaturated sites provided by metalated porphyrin. Precisely, the Cu(II) atom sited at the tetra-pyrrole ring displays a marked Jahn-Teller effect [39] which endows the metal center with the capability to interact with the reaction intermediates through easily reversible coordination bonds, lengthening, as a consequence, their permanence close to the metal site and favoring the formation of more reduced species. The performance worsening relative to TCPP content can be explained based on the lower amount of Cu-TCPP complex in Cu@TCPP_0.01, while in Cu@TCPP_1, it can be related to the competitive light-absorption occurring between free- and metalated porphyrins, which coexist at a ratio of *ca.* 0.5, in such a way that photons absorbed by the free-base porphyrin are wasted by luminescent decay and do not contribute so efficiently to the continuous photoreduction of CO$_2$.

All in all, since the MOA lacking TCPP is also capable of producing meaningful amounts of alcohols [12], the overall photo-catalytic performance of Cu@TCPP MOAs seems to arise from the combined contribution of Ti-oxocluster/NH$_2$BDC and Ti-oxocluster/TCPP(Cu) ensembles. It deserves to be noted that the analogous microporous MIL-125-NH$_2$ has been described as metal clusters and organic ligands behaving as isolated semiconductor quantum dots and light-harvesting antennas, respectively, in such a way that the highest occupied states (valence band maximum, VBM) are localized in the aromatic ligands (NH$_2$BDC; mainly comprised by the π-electron cloud), while the lowest unoccupied states (conduction band minimum, CBM) are sited in the octameric clusters (consisting of empty 3d-orbitals of Ti(IV)). The reduction half-reaction happens in this case through the photoelectron promoted to empty d-orbitals of titanium upon light irradiation, while the holes lead the complementary oxidation half-reaction. In this sense, MIL-125-NH$_2$ presents CBM and VBM values of −2.78 and −5.46 eV in the absolute scale (−1.66 and 1.02 V in the SHE scale), respectively [56], which at pH = 7 provide the necessary driving force to conduct the CO$_2$ reduction reaction (−0.38 and −0.33 V for methanol and ethanol, respectively) [57] and the oxygen evolution reaction (OER; −0.81 V) (see Fig. S14). In fact,

superior performance in terms of the overall alcohol reaction rate (422 μmol·g^{-1}·h^{-1}) and apparent quantum yield (AQY = 11%) [12]. Therefore, incorporating neat porphyrin at low concentrations did not yield any benefit. This outcome can be related to the high extinction coefficient of the TCPP ligand, which absorbs to a great extent the photons reaching the catalyst, but the resulting photo-electrons, prior to reaction, decay radiatively upon short lifetimes (a few nanoseconds) [53]. As a result, the AQY is reduced respect to the porphyrin-free MOA. In contrast, when the porphyrin content is increased (TCPP_0.1 and TCPP_1), the performance meaningfully improves (AQY$_{alchohols}$ = 7 and 5%, respectively), producing meth-anol as the major product (r_{CH3OH} = 332 and 200 μmol·g^{-1}·h^{-1}) and ethanol in lower yields (r_{C2H5OH} = 36 and 27 μmol·g^{-1}·h^{-1}). This enhancement can be explained based on the fact that the in-crease in porphyrin concentration within the solid lengthens the

Table 4
Porosity data for neat and Cu(II)-metalated MOAs.[a]

Sample	S_{BET} (m^2·g^1)	S_{micro} (m^2·g^1)	S_{ext} (m^2·g^1)	V_{micro} (cm^3·g^1)	V_{meso} (cm^3·g^{-1})	V_{macro} (cm^3·g^{-1})	D_{probed} (nm)
TCPP_0.01	651	41	610	0.010	1.248	5.725	≤170
TCPP_0.1	613	39	574	0.009	1.123	6.584	≤174
TCPP _1	822	119	703	0.046	1.462	5.623	≤163
Cu@TCPP_0.01	512	0	512	0	0.961	5.786	≤175
Cu@TCPP_0.1	564	0	564	0	1.069	5.863	≤176
Cu@TCPP_1	686	86	600	0.033	1.323	6.782	≤175

[a] S_{BET} stands for BET specific surface area. Micropore surface area (S_{micro}) and volume (V_{micro}) are estimated from the t-plot calculation. External surface area is calculated by subtracting the microporous contribution from the total area (S_{ext} = S_{BET} − S_{micro}), V_{meso} is the extracted pore volume for pores ≤50 nm, subtracting the contribution of micropore volume, and V_{macro} is calculated by subtracting V_{micro} and V_{meso} from the total void volume for pores below the maximum probed pore-size (D_{probed}).
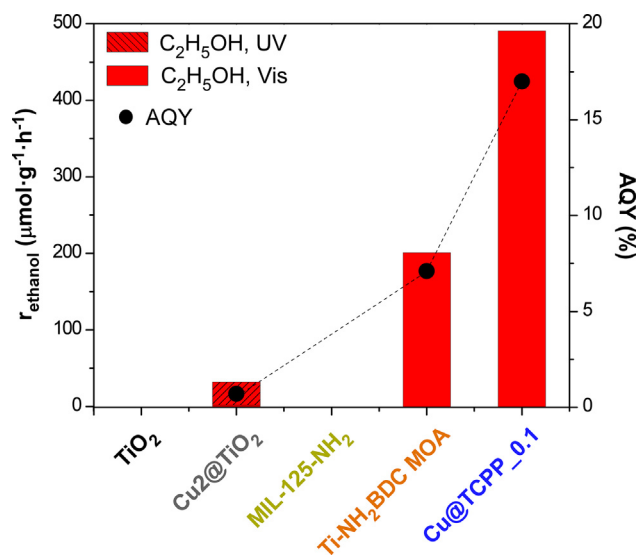
Fig. 10. (a) Reaction rates (r, bars) and apparent quantum yield (AQY, dots) at 180 min in the continuous photoreduction of CO_2 for the prepared MOAs-based surfaces under visible light for methanol and ethanol production. (b) Evolution of the photocatalytic performance during 6 h of continuous operation for Cu@TCPP_0.1.

radiation), and when a 400 nm cut-off filter is employed (i.e. using only visible radiation), the yield goes down until 108 $\mu mol \cdot g^{-1} \cdot h^{-1}$ [65]. Considering metal-organic materials, the introduction of Au nanoparticles in ZIF-67 provides outstanding methanol (2500–3160 $\mu mol \cdot g^{-1} \cdot h^{-1}$) and high ethanol (480–500 $\mu mol \cdot g^{-1} h^{-1}$) production rates while using triethanol-amine as a hole scavenger (sacrificial agent) and also under solar-simulation conditions [6]. The next best ethanol production rate for metal-organic materials is achieved under UV–Vis irradiation of a xenon lamp and without hole scavenger using gC_3N_4/CuO@-MIL125(Ti) composite (501.9 $\mu mol \cdot g^{-1} \cdot h^{-1}$) [66]. Both latter values are comparable to the ethanol production rate of the herein presented Cu@TCPP_0.1 MOA (491 $\mu mol \cdot g^{-1} \cdot h^{-1}$), with the difference that the MOA is a purely metal-organic material, the process is conducted in aqueous solution without the addition of a sacrificial agent, and experiments are performed only under visible radiation. Furthermore, quantum yield for ethanol production is higher than that reported for Au@ZIF-67 (17% MOA vs. 7% MOF-composite), while no AQY data was reported for gC_3N_4/CuO@MIL125(Ti).

In any case, the comparison of the performance of different photocatalysts cannot be exclusively reduced to the nature of the material and to the features of the light irradiation since the type of reactor and reaction conditions can largely influence the results [26]. Most of the above-mentioned reactors consist of slurry batch reactors, while the current study has employed an opto-fluidic microreactor that allows continuous CO_2 conversion. Accordingly, Fig. 11 compares the ethanol production rates of the best-performing Cu@TCPP_0.1 with respect to the rates provided by other previously published photocatalysts [12,27] using the same type of reactor and reaction conditions, except for the type of light used (the values for TiO_2 and Cu@TiO_2 have been obtained under UV LED light, while in the remaining cases visible white LED light has been employed). Once again, the ethanol production rates obtained with the TCPP(Cu) functionalized titanium(IV) metal-organic aerogel beat by far the performance of the referential inorganic and metal-organic catalysts, while the achieved greater AQY values indicate a better exploitation of the light.

previous works dealing with MIL-125-NH_2 type materials showed that Ti-oxocluster/NH_2BDC ensembles are also able to conduct both (1) CO_2 reduction without using a sacrificial agent [10,12] and (2) water splitting reactions [58,59]. In the latter case, the analyzed Ti-oxocluster/NH_2BDC ensembles present CBM and VBM values suitable for the complementary HER and OER in water splitting, and accordingly, hydrogen and oxygen formation are experimentally observed upon 450 nm visible light illumination. The referenced work also states that defects that imply the replacement of carboxylate linkers by hydroxides (such as the ones present in MOAs) can improve the photocatalytic response of the material.

The stability of the best-performing photocatalytic material (Cu@TCPP_0.1 MOA) was assessed for 6 h of continuous operation under visible light (Fig. 10b). The results show roughly stable values for methanol and ethanol production rates and apparent quantum yields. Besides, as far as we are aware, Cu@TCPP_0.1 MOA outperforms any of the up-to-date reported ethanol production rates and AQY values for the CO_2 photocatalytic reduction reaction performed under visible-light illumination and without any sacrificial agent. In the case of inorganic photocatalysts, most of the best-performing ones in CO_2-to-ethanol conversion are composed of transition metal-doped TiO_2 samples that yield activities ranging between 42 and 271 $\mu mol \cdot g^{-1} \cdot h^{-1}$ [27,60−66]. The so far highest reported value corresponds to $BiVO_4$, in its monoclinic phase, which provides selectively ethanol with a production rate of 2033 $\mu mol \cdot g^{-1} \cdot h^{-1}$ under solar simulation conditions (UV−Vis

Fig. 11. Production rate and AQY values for the CO_2-to-ethanol photocatalytic conversion using the same type of optofluidic microreactor. Data for TiO_2-based materials, MIL-125-NH_2, and analogous Ti−NH_2-BDC MOAs were taken from the literature [12,27].

4. Conclusions

The fine tuning of the synthesis conditions allowed to yield a novel family of metal-organic gels functionalized with TCPP in ratios with respect to the metal-clusters close to 0.01, 0.1 and 1. The supercritical drying of the gels provided highly porous aerogels comprised of crosslinked metal-organic nanoparticles (5–10 nm) with surface area values ranging from 600 to 800 $m^2 \cdot g^{-1}$. The post-synthetic modification of the coordination framework allowed to metalate the tetrapyrrole ring of the TCPP ligand with Cu(II), as demonstrated by the combination of chemical and spectroscopic analyses. Accordingly, the TCPP(Cu) complex formation is evidenced by the quenching of the two fluorescence maxima due to the intramolecular charge transfer implying the partially filled $3d_{x^2-y^2}$ orbital of copper(II). Besides, prior to metalation, the DRS-UV-Vis absorption spectra of MOAs show the four characteristic Q bands of free-base porphyrins (TCPP(H_2)) with a D_{2h} point group, arising from HOMO → LUMO and HOMO−1 → LUMO transitions, while the metalation with Cu(II) produces a decay of the former set of bands and the emergence of two new Q bands ascribed to the D_{4h} symmetry adopted by the porphyrin upon the formation of the TCPP(Cu) complex. Interestingly, the Soret bands (400–500 nm) and Q bands (545–590 nm) of observable metalated MOAs fit well into the visible emission spectra provided by the LED array selected for the photocatalytic experiments, which could favor a more efficient utilization of the light.

Regarding the CO_2 photoreduction experiments, the post-synthetic metalation with Cu(II) markedly invigorates the total alcohol (methanol and ethanol) production rates and apparent quantum yields (AQY), from 21–367 $\mu mol \cdot g^{-1} \cdot h^{-1}$ (AQY: 0.4–7%) prior to metalation to values of 356–642 $\mu mol \cdot g^{-1} \cdot h^{-1}$ (AQY: 11–20%), respectively. This improvement is probably related to the fact that the produced photoelectrons in the parent MOAs containing free-base porphyrin, prior to reaction, decay radiatively upon short lifetimes (few nanoseconds), while the post-synthetic metalation of the MOAs inhibits the radiative decay, which can lengthen the lifespan of the charges and leave the photoelectron ready to react on the copper atom by means of the ligand-to-metal charge transfer mechanism. Another remarkable result related to the post-synthetic modification lies in the flipping of the selectivity towards ethanol, which changes from 0–12% in pristine MOA to 67–76% after Cu(II)-metalation. As a result, the best-performing Cu@TCPP_0.1 MOA surpasses any of the up-to-date reported ethanol production rates and AQY values for CO_2 photocatalytic reduction reactions performed under visible-light illumination and without sacrificial agents. Note that CO_2 reduction to ethanol is mechanistically more demanding than methanol and its market size is greater, which makes the progress in photocatalytic ethanol production in the context of circular chemistry highly appealing.

Credit authorship contribution statement

G.B., M.P.-I, and S.P.-Y. conceived the experiments and wrote the manuscript. M.P.-I, I. M.-G, J.A. and O.C. conducted the synthesis, characterizations, and photocatalytic experiments; M. P.-I, I. M.-G, J.A., O.C., G.B., A.L. and S.P.-Y. analyzed the results. All authors reviewed the manuscript.

Declaration of competing interest

The authors declare the following financial interests/personal relationships which may be considered as potential competing interests:

Garikoitz Beobide reports equipment, drugs, or supplies and travel were provided by Spanish Ministry of Science and Innovation. Oscar Castillo reports equipment, drugs, or supplies and travel were provided by Spanish Ministry of Science and Innovation. Jonathan Albo reports equipment, drugs, or supplies and travel were provided by Spanish Ministry of Science and Innovation. Maite Perfecto-Irigaraya reports financial support was provided by University of the Basque Country.

Data availability

Data will be made available on request.

Appendix A. Supplementary data

Supplementary data to this article can be found online at https://doi.org/10.1016/j.mtener.2023.101346.

References

[1] 2021 United Nations Climate Change Conference, COP26, Glasgow, (n.d.). http://www.ukcop26.org (accessed 24 March 2022).

[2] European Green Deal. https://commission.europa.eu/strategy-and-policy/priorities-2019-2024/european-green-deal (accessed 22 March 2023).

[3] G. Centi, S. Perathoner, Opportunities and prospects in the chemical recycling of carbon dioxide to fuels, Catal. Today 148 (2009) 191−205, https://doi.org/10.1016/j.cattod.2009.07.075.

[4] T. Keijer, V. Bakker, J.C. Slootweg, Circular chemistry to enable a circular economy, Nat. Chem. 11 (2019) 190−195, https://doi.org/10.1038/s41557-019-0226-9.

[5] F.O. Ochedi, D. Liu, J. Yu, A. Hussain, Y. Liu, Photocatalytic, electrocatalytic and photoelectrocatalytic conversion of carbon dioxide: a review, Environ. Chem. Lett. 19 (2021) 941−967, https://doi.org/10.1007/s10311-020-01131-5.

[6] J. Becerra, D.-T. Nguyen, V.-N. Gopalakrishnan, T.-O. Do, Plasmonic Au nanoparticles incorporated in the zeolitic imidazolate framework (ZIF-67) for the efficient sunlight-driven photoreduction of CO_2, ACS Appl. Energy Mater. 3 (2020) 7659−7665, https://doi.org/10.1021/acsaem.0c01083.

[7] J. Becerra, V.N. Gopalakrishnan, T.-A. Quach, T.-O. Do, Enhancing CO_2 photoreduction over ZIF-based reticular materials by morphology control of Au plasmonic nanoparticles, Sustain. Energy Fuels 6 (2022) 449−457, https://doi.org/10.1039/D1SE01890F.

[8] J.O. Olowoyo, U. Saini, M. Kumar, H. Valdés, H. Singh, M.O. Omorogie, J.O. Babalola, A.V. Vorontsov, U. Kumar, P.G. Smirniotis, Reduced graphene oxide/NH_2-MIL-125(Ti) composite: selective CO_2 photoreduction to methanol under visible light and computational insights into charge separation, J. CO2 Util. 42 (2020), 101300, https://doi.org/10.1016/J.JCOU.2020.101300.

[9] Y. Liu, Y. Yang, Q. Sun, Z. Wang, B. Huang, Y. Dai, X. Qin, X. Zhang, Chemical adsorption enhanced CO_2 capture and photoreduction over a copper porphyrin based metal-organic framework, ACS Appl. Mater. Interf. 5 (2013) 7654−7658, https://doi.org/10.1021/am4019675.

[10] J. Meng, Q. Chen, J. Lu, H. Liu, Z-scheme photocatalytic CO_2 reduction on a heterostructure of oxygen-defective ZnO/reduced graphene oxide/UiO-66-NH_2 under visible light, ACS Appl. Mater. Interf. 11 (2018) 550−562, https://doi.org/10.1021/acsami.8b14282.

[11] Y. Su, Z. Zhang, H. Liu, Y. Wang, $Cd_{0.2}Zn_{0.8}$S@UiO-66-NH_2 nanocomposites as efficient and stable visible-light-driven photocatalyst for H_2 evolution and CO_2 reduction, Appl. Catal. B Environ. 200 (2017) 448−457, https://doi.org/10.1016/J.APCATB.2016.07.032.

[12] A. Angulo-Ibáñez, M. Perfecto-Irigaray, I. Merino-Garcia, N. Luengo, A.M. Goitandia, J. Albo, E. Aranzabe, G. Beobide, O. Castillo, S. Pérez-Yáñez, Metal-organic aerogels based on titanium(IV) for visible-light conducted CO_2 photoreduction to alcohols, Mater. Today Energy 30 (2022), 101178, https://doi.org/10.1016/j.mtener.2022.101178.

[13] J. Hou, A.F. Sapnik, T.D. Bennett, Metal−organic framework gels and monoliths, Chem. Sci. 11 (2020) 310−323, https://doi.org/10.1039/C9SC04961D.

[14] M. Perfecto-Irigaray, G. Beobide, S. Calero, O. Castillo, I. da Silva, J.J. Gutierrez Sevillano, A. Luque, S. Pérez-Yáñez, L.F. Velasco, Metastable Zr/Hf-MOFs: the hexagonal family of EHU-30 and their water-sorption induced structural transformation, Inorg. Chem. Front. 8 (2021) 4767−4779, https://doi.org/10.1039/D1QI00997D.

[15] L. Zou, R. Sa, H. Lv, H. Zhong, R. Wang, Recent advances on metalloporphyrin-based materials for visible-light-driven CO2 reduction, ChemSusChem (2020), https://doi.org/10.1002/cssc.202001796.

[16] B.B. Beyene, C.-H. Hung, Recent progress on metalloporphyrin-based hydrogen evolution catalysis, Coord. Chem. Rev. 410 (2020), 213234, https://doi.org/10.1016/j.ccr.2020.213234.

[17] C. Zlotea, D. Phanon, M. Mazaj, D. Heurtaux, V. Guillerm, C. Serre, P. Horcajada, T. Devic, E. Magnier, F. Cuevas, G. Férey, P.L. Llewellyn, M. Latroche, Effect of NH2 and CF3 functionalization on the hydrogen sorption properties of MOFs, J. Chem. Soc. Dalt. Trans. 40 (2011) 4879−4881, https://doi.org/10.1039/c1dt10115c.

[18] S. Brunauer, P.H. Emmett, E. Teller, Adsorption of gases in multimolecular layers, J. Am. Chem. Soc. 60 (1938) 309−319, https://doi.org/10.1021/ja01269a023.

[19] J. Rouquerol, P. Llewellyn, F. Rouquerol, Is the BET equation applicable to microporous adsorbents?, in: Stud. Surf. Sci. Catal. Elsevier B.V., 2007, pp. 49−56.

[20] K. Sumida, D.L. Rogow, J.A. Mason, T.M. McDonald, E.D. Bloch, Z.R. Herm, T.-H. Bae, J.R. Long, Carbon dioxide capture in metal−organic frameworks, Chem. Rev. 112 (2012) 724−781, https://doi.org/10.1021/cr2003272.

[21] H. Pan, J.A. Ritter, P.B. Balbuena, Isosteric heats of adsorption on carbon predicted by density functional theory, Ind. Eng. Chem. Res. 37 (1998) 1159−1166, https://doi.org/10.1021/ie9705867.

[22] B.C. Lippens, J.H. Boer, Studies on pore systems in catalysts V. The t method, J. Catal. 4 (1965) 319−323.

[23] F. Rouquerol, J. Rouquerol, K. Sing, Adsorption by Powders and Porous Solids. Principles, Methodology and Applications, Elsevier, 1999, https://doi.org/10.1016/B978-0-12-598920-6.X5000-3.

[24] F. Munk Kubelka, A contribution to the optics of pigments, Z. Technol. Phys. 12 (1931) 593−599.

[25] P. Makuła, M. Pacia, W. Macyk, How to correctly determine the band gap energy of modified semiconductor photocatalysts based on UV-Vis spectra, J. Phys. Chem. Lett. 9 (2018) 6814−6817, https://doi.org/10.1021/acs.jpclett.8b02892.

[26] I. Merino-Garcia, G. García, I. Hernández, J. Albo, An optofluidic planar microreactor with photoactive Cu2O/Mo2C/TiO2 heterostructures for enhanced visible light-driven CO2 conversion to methanol, J. CO2 Util. 67 (2023), 102340, https://doi.org/10.1016/j.jcou.2022.102340.

[27] J. Albo, M.I. Qadir, M. Samperi, J.A. Fernandes, I. de Pedro, J. Dupont, Use of an optofluidic microreactor and Cu nanoparticles synthesized in ionic liquid and embedded in TiO2 for an efficient photoreduction of CO2 to methanol, Chem. Eng. J. 404 (2021) 126643, https://doi.org/10.1016/j.cej.2020.126643.

[28] L. Patiny, A. Borel, ChemCalc: a building block for tomorrow's chemical infrastructure, J. Chem. Inf. Model. 53 (2013) 1223−1228, https://doi.org/10.1021/ci300563h.

[29] MassLynx V4.1, 2010, Waters Inc.

[30] S. Wang, H. Reinsch, N. Heymans, M. Wahiduzzaman, C. Martineau-Corcos, G. De Weireld, G. Maurin, C. Serre, Toward a rational design of titanium metal-organic frameworks, Matter 2 (2020) 440−450, https://doi.org/10.1016/j.matt.2019.11.002.

[31] H. Assi, G. Mouchaham, N. Steunou, T. Devic, C. Serre, Titanium coordination compounds: from discrete metal complexes to metal−organic frameworks, Chem. Soc. Rev. 46 (2017) 3431−3452, https://doi.org/10.1039/C7CS00001D.

[32] S. Yuan, J.-S. Qin, C.T. Lollar, H.-C. Zhou, Stable metal−organic frameworks with group 4 metals: current status and trends, ACS Cent. Sci. 4 (2018) 440−450, https://doi.org/10.1021/acscentsci.8b00073.

[33] A.P. Smalley, D.G. Reid, J.C. Tan, G.O. Lloyd, Alternative synthetic methodology for amide formation in the post-synthetic modification of Ti-MIL125-NH2, CrystEngComm 15 (2013) 9368−9371, https://doi.org/10.1039/c3ce41332b.

[34] S. Yuan, T.F. Liu, D. Feng, J. Tian, K. Wang, J. Qin, Q. Zhang, Y.P. Chen, M. Bosch, L. Zou, S.J. Teat, S.J. Dalgarno, H.C. Zhou, A single crystalline porphyrinic titanium metal-organic framework, Chem. Sci. 6 (2015) 3926−3930, https://doi.org/10.1039/c5sc00916b.

[35] G. Lan, K. Ni, S.S. Veroneau, X. Feng, G.T. Nash, T. Luo, Z. Xu, W. Lin, Titanium-based nanoscale metal-organic framework for type I photodynamic therapy, J. Am. Chem. Soc. 141 (2019) 4204−4208, https://doi.org/10.1021/jacs.8b13804.

[36] Q.R. Ding, G.L. Xu, L. Zhang, J. Zhang, Ligand-directed assembly engineering of trapezoidal {Ti5} building blocks stabilized by dimethylglyoxime, Dalt. Trans. 48 (2019) 9916−9919, https://doi.org/10.1039/c9dt02032b.

[37] Y. Ma, X. Han, S. Xu, Z. Wang, W. Li, I. da Silva, S. Chansai, D. Lee, Y. Zou, M. Nikiel, P. Manuel, A.M. Sheveleva, F. Tuna, E.J.L. McInnes, Y. Cheng, S. Rudić, A.J. Ramirez-Cuesta, S.J. Haigh, C. Hardacre, M. Schröder, S. Yang, Atomically dispersed copper sites in a metal−organic framework for reduction of nitrogen dioxide, J. Am. Chem. Soc. 143 (2021) 10977−10985, https://doi.org/10.1021/jacs.1c03036.

[38] M.-S. Liao, S. Scheiner, Electronic structure and bonding in metal porphyrins, metal=Fe, Co, Ni, Cu, Zn, J. Chem. Phys. 117 (2002) 205−219, https://doi.org/10.1063/1.1480872.

[39] K.N. Solo'ev, V.N. Knyukshto, G.D. Egorova, New features of the phosphorescence of copper complexes of meso-trtraarylporphyrins, J. Appl. Spectrosc. 66 (1999) 743−747.

[40] R. Giovannetti, The Use of spectrophotometry UV-Vis for the study of porphyrins, in: Macro to Nano Spectrosc., InTechOpen, London, United Kingdom, 2012, https://doi.org/10.5772/38797.

[41] M. Gouterman, Spectra of porphyrins, J. Mol. Spectrosc. 6 (1961) 138−163, https://doi.org/10.1016/0370-2693(87)90819-7.

[42] M. Gouterman, Study of the effects of substitution on the absorption spectra of porphin, J. Chem. Phys. 30 (1959) 1139−1161, https://doi.org/10.1063/1.1730148.

[43] Y. Fu, H. Yang, R. Du, G. Tu, C. Xu, F. Zhang, M. Fan, W. Zhu, Enhanced photocatalytic CO2 reduction over Co-doped NH2-MIL-125(Ti) under visible light, RSC Adv. 7 (2017) 42819−42825, https://doi.org/10.1039/C7RA06324E.

[44] P. J. Linstrom, W. G. Mallard, NIST Chemistry WebBook, NIST Standard Reference Database Number 69, Natl. Inst. Stand. Technol. Gaithersbg. MD, 20899, (accessed: November 2022).

[45] K. Zhu, M. Zhang, X. Feng, L. Qin, S.-Z. Kang, X. Li, A novel copper-bridged graphitic carbon nitride/porphyrin nanocomposite with dramatically enhanced photocatalytic hydrogen generation, Appl. Catal. B Environ. 268 (2020), 118434, https://doi.org/10.1016/j.apcatb.2019.118434.

[46] R.R. Solís, A. Gómez-Avilés, C. Belver, J.J. Rodriguez, J. Bedia, Microwave-assisted synthesis of NH2-MIL-125(Ti) for the solar photocatalytic degradation of aqueous emerging pollutants in batch and continuous tests, J. Environ. Chem. Eng. 9 (2021) 106230, https://doi.org/10.1016/j.jece.2021.106230.

[47] H. Yamashige, S. Matsuo, T. Kurisaki, R.C.C. Perera, H. Wakita, Local structure of nitrogen atoms in a porphine ring of meso-phenyl substituted porphyrin with an electron-withdrawing group using X-ray photoelectron spectroscopy and X-ray absorption spectroscopy, Anal. Sci. 21 (2005) 635−639, https://doi.org/10.2116/analsci.21.635.

[48] M. Thommes, K. Kaneko, A.V. Neimark, J.P. Olivier, F. Rodriguez-Reinoso, J. Rouquerol, K.S.W. Sing, Physisorption of gases, with special reference to the evaluation of surface area and pore size distribution (IUPAC Technical Report), Pure Appl. Chem. 87 (2015) 1051−1069, https://doi.org/10.1515/pac-2014-1117.

[49] L. Li, X. Wang, T. Liu, J. Ye, Titanium-based MOF materials: from crystal engineering to photocatalysis, Small Methods 4 (2020), 2000486, https://doi.org/10.1002/smtd.202000486.

[50] J. Santos-Lorenzo, R. San José-Velado, J. Albo, G. Beobide, P. Castaño, O. Castillo, A. Luque, S. Pérez-Yáñez, A straightforward route to obtain zirconium based metal-organic gels, Microporous Mesoporous Mater. 284 (2019) 128−132, https://doi.org/10.1016/j.micromeso.2019.04.008.

[51] L. Liu, Y. Li, Understanding the reaction mechanism of photocatalytic reduction of CO2 with H2O on TiO2-based photocatalysts: a review, Aerosol Air Qual. Res. 14 (2014) 453−469, https://doi.org/10.4209/aaqr.2013.06.0186.

[52] J. Albo, G. García, Enhanced visible-light photoreduction of CO2 to methanol over Mo2 C/TiO2 surfaces in an optofluidic microreactor, React. Chem. Eng. 6 (2021) 304−312, https://doi.org/10.1039/D0RE00376J.

[53] I.E. Kolesnikov, A.A. Kalinichev, M.A. Kurochkin, E.Y. Kolesnikov, E. Lähderanta, Porphyrins as efficient ratiometric and lifetime-based contactless optical thermometers, Mater. Des. 184 (2019), 108188, https://doi.org/10.1016/j.matdes.2019.108188.

[54] H.-J. Son, S. Jin, S. Patwardhan, S.J. Wezenberg, N.C. Jeong, M. So, C.E. Wilmer, A.A. Sarjeant, G.C. Schatz, R.Q. Snurr, O.K. Farha, G.P. Wiederrecht, J.T. Hupp, Light-harvesting and ultrafast energy migration in porphyrin-based metal−organic frameworks, J. Am. Chem. Soc. 135 (2013) 862−869, https://doi.org/10.1021/ja310596a.

[55] S.S. Rajasree, X. Li, P. Deria, Physical properties of porphyrin-based crystalline metal−organic frameworks, Commun. Chem. 4 (2021) 47, https://doi.org/10.1038/s42004-021-00484-4.

[56] Y. Li, Y. Fu, B. Ni, K. Ding, W. Chen, K. Wu, X. Huang, Y. Zhang, Effects of ligand functionalization on the photocatalytic properties of titanium-based MOF: a density functional theory study, AIP Adv. 8 (2018), 035012, https://doi.org/10.1063/1.5021098.

[57] A. Sartorel, M. Bonchio, S. Campagna, F. Scandola, Tetrametallic molecular catalysts for photochemical water oxidation, Chem. Soc. Rev. 42 (2013) 2262−2280, https://doi.org/10.1039/C2CS35287G.

[58] S. Remiro-Buenamañana, M. Cabrero-Antonino, M. Martínez-Guanter, M. Álvaro, S. Navalón, H. García, Influence of co-catalysts on the photocatalytic activity of MIL-125(Ti)-NH2 in the overall water splitting, Appl. Catal. B Environ. 254 (2019) 677−684, https://doi.org/10.1016/j.apcatb.2019.05.027.

[59] M. Cabrero-Antonino, J. Albero, C. García-Vallés, M. Álvaro, S. Navalón, H. García, Plasma-induced defects enhance the visible-light photocatalytic activity of MIL-125(Ti)-NH 2 for overall water splitting, Chem. Eur J. 26 (2020) 15682−15689, https://doi.org/10.1002/chem.202003763.

[60] N. Lertthanaphol, N. Prawiset, P. Soontornapaluk, N. Kitjanukit, W. Neamsung, N. Pienutsa, K. Chusri, T. Sornsuchat, P. Chanthara, P. Phadungbut, P. Seeharaj, P. Kim-Lohsoontorn, S. Srinives, Soft template-assisted copper-doped sodium dititanate nanosheet/graphene oxide heterostructure for photoreduction of carbon dioxide to liquid fuels, RSC Adv. 12 (2022) 24362−24373, https://doi.org/10.1039/D2RA04283E.

[61] L.M. Pastrana-Martínez, A.M.T. Silva, N.N.C. Fonseca, J.R. Vaz, J.L. Figueiredo, J.L. Faria, Photocatalytic reduction of CO_2 with water into methanol and ethanol using graphene derivative−TiO_2 composites: effect of pH and copper(I) oxide, Top. Catal. 59 (2016) 1279−1291, https://doi.org/10.1007/s11244-016-0655-2.

[62] N. Lertthanaphol, N. Pienutsa, K. Chusri, T. Sornsuchat, P. Chanthara, P. Seeharaj, P. Kim-Lohsoontorn, S. Srinives, One-step hydrothermal synthesis of precious metal-doped titanium dioxide−graphene oxide composites for photocatalytic conversion of CO_2 to ethanol, ACS Omega 6 (2021) 35769−35779, https://doi.org/10.1021/acsomega.1c05799.

[63] P. Seeharaj, P. Kongmun, P. Paiplod, S. Prakobmit, C. Sriwong, P. Kim-Lohsoontorn, N. Vittayakorn, Ultrasonically-assisted surface modified TiO_2/rGO/CeO_2 heterojunction photocatalysts for conversion of CO_2 to methanol and ethanol, Ultrason. Sonochem. 58 (2019), 104657, https://doi.org/10.1016/j.ultsonch.2019.104657.

[64] N.-N. Vu, C.-C. Nguyen, S. Kaliaguine, T.-O. Do, Reduced Cu/Pt-H$Ca_2Ta_3O_{10}$ perovskite nanosheets for sunlight-driven conversion of CO_2 into valuable fuels, Adv. Sustain. Syst. 1 (2017), 1700048, https://doi.org/10.1002/adsu.201700048.

[65] Y. Liu, B. Huang, Y. Dai, X. Zhang, X. Qin, M. Jiang, M.-H. Whangbo, Selective ethanol formation from photocatalytic reduction of carbon dioxide in water with $BiVO_4$ photocatalyst, Catal. Commun. 11 (2009) 210−213, https://doi.org/10.1016/j.catcom.2009.10.010.

[66] N. Li, X. Liu, J. Zhou, W. Chen, M. Liu, Encapsulating CuO quantum dots in MIL-125(Ti) coupled with g-C_3N_4 for efficient photocatalytic CO_2 reduction, Chem. Eng. J. 399 (2020), 125782, https://doi.org/10.1016/j.cej.2020.125782.